Geophysical Research Letters

RESEARCH LETTER
10.1029/2019GL082256

Orographic Primary and Secondary Gravity Waves in the Middle Atmosphere From 16-Year SABER Observations

Xiao Liu[1,2], **Jiyao Xu**[2,3], **Jia Yue**[4], **Sharon L. Vadas**[5], **and Erich Becker**[6]

[1]Henan Engineering Laboratory for Big Data Statistical Analysis and Optimal Control, School of Mathematics and Information Science, Henan Normal University, Xinxiang, China, [2]State Key Laboratory of Space Weather, National Space Science Center, Chinese Academy of Sciences, Beijing, China, [3]College of Earth Science, University of Chinese Academy of Science, Beijing, China, [4]Atmospheric and Planetary Sciences, Hampton University, Hampton, VA, USA, [5]Northwest Research Associates, Boulder, CO, USA, [6]Leibniz Institute of Atmospheric Physics, Kühlungsborn, Germany

Key Points:
- Orographic primary and larger-scale secondary gravity waves are observed in the middle atmosphere using SABER observations from 2002–2017
- Over the southern Andes, secondary GWs are generated from MW breaking in the upper stratosphere from April to October and have a westward tilt with height
- At around 40°N and 20°N in the NH summer and 20°S in the NH winter and autumn, the GW peaks coincide with topographic peaks

Correspondence to:
X. Liu,
liuxiao@htu.edu.cn

Citation:
Liu, X., Xu, J., Yue, J., Vadas, S. L., & Becker, E. (2019). Orographic primary and secondary gravity waves in the middle atmosphere from 16-year SABER observations. *Geophysical Research Letters*, *46*. https://doi.org/10.1029/2019GL082256

Received 28 JAN 2019
Accepted 3 APR 2019
Accepted article online 10 APR 2019

Abstract The seasonal and height dependencies of the orographic primary and larger-scale secondary gravity waves (GWs) have been studied using the temperature profiles measured by Sounding of the Atmosphere using Broadband Emission Radiometry (SABER) from 2002 to 2017. At ~40°S and during Southern Hemisphere winter, there is a strong GW peak over the Andes mountains that extend to $z \sim 55$ km. Using wind and topographic data, we show that orographic GWs break above the peak height of the stratospheric jet. At $z \sim 55$–65 km, GW breaking and momentum deposition create body forces that generate larger-scale secondary GWs; we show that these latter GWs form a wide peak above 65 km with a westward tilt. At middle latitudes during summer in the respective hemisphere, orographic GW breaking also generates larger-scale secondary GWs that propagate to higher altitudes. Both orographic primary and larger-scale secondary GWs are likely responsible for most of the non-equatorial peaks of the persistent global distribution of GWs in SABER.

Plain Language It is important to characterize orographic primary gravity waves (GWs) and the larger-scale secondary GWs via both observations and numerical modeling because of their role in dynamics of the atmosphere. We present the global distributions of GWs and the associated larger-scale secondary GWs in the middle atmosphere ($z \sim 30$–100 km) from temperature profiles measured by the SABER instrument over the past 16 years (2002–2017). We show that the peaks of the primary and the associated secondary GWs coincide with topographic peaks and that these associations depend on latitude and season. The polar stratospheric jet and the lower stratospheric wind reversal cause the orographic GWs break. The breaking GWs deposit their momentum and induce body forces that generate larger-scale secondary GWs; these secondary GWs are responsible for the GWs peaks observed above the mountain wave breaking height.

1. Introduction

Gravity waves (GWs) can be generated through various sources, for example, flow over topography, wind jet or shear, and convection (Fritts & Alexander, 2003). As GWs propagate upward, they are influenced by the environment and modulate the atmospheric structure through transportation and deposition of momentum and energy both vertically and horizontally (Alexander et al., 2010; Becker & Vadas, 2018; Ern et al., 2011, 2014; Ern & Preusse, 2012; Geller et al., 2013; Liu, 2000, 2016; Liu et al., 2008, 2018; Liu & Vadas, 2013; Vadas et al., 2014). Due to the propagation of GWs and their interactions with the background atmosphere, primary GWs can break, thereby creating some combination of small-scale GWs and turbulence. These small-scale secondary GWs have horizontal wavelengths (λ_x) that are smaller than that of the primary GWs and may dissipate into turbulence (Fritts & Alexander, 2003). They then deposit their momentum and energy into the atmosphere on scales of order the primary GWs. The deposited momentum and energy create local body forces and heat/coolings, which result in the radiation of larger-scale secondary GWs (LSW; Vadas, 2013; Vadas et al., 2003; Vadas & Fritts, 2002). These LSWs have λ_x of 4–10 times of the primary GW (depending on the size of the wave packet) and have larger vertical wavelengths (λ_z) and faster phase speeds (Vadas et al., 2003, 2018). They propagate in all azimuths except perpendicular to the body force direction. For those that propagate upward, their amplitudes increase exponentially with height, thereby enabling them to have important influences on the upper atmosphere and ionosphere (Becker & Vadas, 2018; Bossert et al., 2017; Chu et al., 2018; de Wit et al., 2017; Fritts et al., 2016; Heale et al., 2017; Liu & Vadas, 2013; Vadas et al., 2014; Vadas & Becker, 2018; Vadas & Liu, 2009, 2013; Watanabe & Miyahara, 2009; Zhao et al., 2017). Thus, it is important to characterize both the primary GWs and LSWs in both observations and model simulations.

Satellite observations reveal GW hot spots in the troposphere and stratosphere. These GW hot spots are related to either orography or tropical convection and are dependent on the season. From November to February, the GWs in the southern stratosphere have three peaks over South America, South Africa, and North Australia, respectively. From March to October, GWs have peaks over the Andes and Antarctic Peninsula. These GW peaks in the Southern Hemisphere are related to the topography and to the zonal winds, as well as to deep convection. In the Northern Hemisphere (NH), the GW peaks are over North America, Central Eurasia, and south of the Himalayas. The spatial distributions of these GWs have been revealed by satellites observations: the Atmospheric Infrared Sounder (e.g., Alexander & Teitelbaum, 2007, 2011; Gong et al., 2012, 2015; Hoffmann et al., 2013; Hoffmann et al., 2016; Hoffmann & Alexander, 2010), the Microwave Limb Sounder (Jiang et al., 2004; Jiang et al., 2004; Wu & Jiang, 2002), the Cryogenic Infrared Spectrometers and Telescopes for the Atmosphere (Eckermann & Preusse, 1999), the Microwave Limb Sounder instrument and the High Resolution Dynamics Limb Sounder instrument (Alexander et al., 2008; Ern & Preusse, 2012; Wu & Eckermann, 2008), and the Global Positioning System radio occultation (Alexander et al., 2009; Baumgaertner & McDonald, 2007; Hindley et al., 2015).

Satellite observations also revealed the global distributions of GWs in the middle atmosphere, and their implications on the GWs in the thermosphere (Bruinsma & Forbes, 2008; Ern et al., 2011; Forbes et al., 2016; Liu et al., 2017; Park et al., 2014; Trinh et al., 2018). Using the temperature profiles measured by the Sounding of the Atmosphere using Broadband Emission Radiometry (SABER) instrument onboard the Thermosphere, Ionosphere, Mesosphere Energetics and Dynamics satellite in January and July of 2006, Ern et al. (2011) showed that the GW momentum flux had three peaks (around 70°W, 10°E, and 110°E) at 30, 50, and 70 km over the subtropical regions of the summer hemispheres (Figure 9 of their paper). Using the thermospheric density and zonal wind measured by the Gravity Field and Steady-State Ocean Circulation Explorer satellite, Liu, Pedatella, and Hocke (2017) showed that the thermospheric GWs are enhanced greatly over the Andes around June solstice, and that this is likely related to mountain wave (MW) activity (although MWs cannot propagate directly into the thermosphere). Using the thermospheric density measured by the Gravity Field and Steady-State Ocean Circulation Explorer and CHAllenging Minisatellite Payload satellites and the temperature measured by the SABER instrument, Trinh et al. (2018) showed that the GWs in the thermosphere and middle atmosphere correlated well with the winter polar vortex. They suggested that this might be due to primary GWs (generated by topography) breaking at $z \sim 60$–80 km and then generating secondary GWs that would propagate further into the thermosphere.

Using a GW-resolving general circulation model, Sato et al. (2009, 2012) showed that GWs were not uniform in longitude and had peaks eastward of the Southern Andes and the Antarctic Peninsula. They suggested that these GWs were generated by the eastward zonal wind blowing over the topography and then being advected eastward. Becker and Vadas (2018) used a different GW-resolving global circulation model and showed that these orographic GWs could break in the middle atmosphere and then generate LSWs. The LSWs were then responsible for the eastward zonal-mean wind around 60°E and $z \sim 100$ km, which has been simulated by two GW-resolving models (Becker & Vadas, 2018; Watanabe & Miyahara, 2009). These simulation studies illustrate the importance of LSWs on the global circulation. However, the global distributions of the LSWs and their seasonal dependence have not been adequately examined yet.

The focus of this paper is to explore the global distributions of orographic GWs and the associated LSWs in the middle atmosphere (30–100 km). The possible mechanisms are also be explored using topographic and wind data, as well as the linear theory of MWs.

2. Data and Method

The data used in this work are (1) the topographic data from the Global 30 Arc-Second Elevation (GTOPO30); (2) the wind data from the Modern Era Retrospective analysis for Research and Applications 2 (Gelaro et al., 2017; Molod et al., 2015); and (3) the temperature data measured by the SABER instrument (Russell et al., 1999) over 16 years (2002–2017). The temperature accuracy of SABER V2.0 is 1–3 K from 30 to 80 km and 5–10 K from 90 to 100 km as reported at http://saber.gats-inc.com/ website. The random nature of the error in the SABER measurements does not significantly affect the GW profile since the GWs extracted by our method have coherent wave-like structure (see below).

The GW extraction method we use here is the same as that described in Appendix A of Liu et al. (2017). The resolved GWs have λ_z of 5–30 km. Due to the limb scan of the SABER observations, the resolved along track λ_x have a minimum of about 300 km (John & Kumar, 2012; Preusse et al., 2002). The maximal resolved along track λ_x are ~3,200–5,000 km, which are estimated by converting the zonal wavenumber of 8 to the circumference of a zonal circle. Note that the upper limit of 5,000 km is the maximum of what we expect for the smallest-amplitude LSWs in the tail of the distribution; indeed, most of the LSWs have λ_x of 1,000–2,500 km (Becker & Vadas, 2018; Vadas & Becker, 2018). From each GW profile, we determine the profile of GW potential energy per unit mass (PE). We then average the daily PE profiles if they fall into a bin of 5° × 20° (latitude × longitude) and get an averaged PE profile in each bin. The bins have an overlap of 2.5° in latitude and 10° in longitude, respectively. We concentrate on the GW PE from 50°S to 50°N.

3. Global Distributions of the Primary and Larger-Scale Secondary GWs

To illustrate the global distributions of the primary and larger-scale secondary GWs, as well as their latitudinal and seasonal dependencies, we decompose the global GW PE into five latitude bands and four seasons. The five latitude bands are 40°S (50–30°S), 20°S (30–10°S), equator (10°S to 10°N), 20°N (10–30°N), and 40°N (30–50°N). The four seasons are the NH spring (March, April, and May), NH summer (June, July, and August), NH autumn (September, October, and November), and NH winter (December, January, and February).

3.1. The Primary and Larger-Scale Secondary GWs at 40°S

The GW PE in the latitude band of 40°S is taken as an example to illustrate the longitudinal variation of both the primary GWs and the LSWs. This is because the Southern Andes mountains are included in this latitude band and result in a large wintertime GW hot spot (Becker & Vadas, 2018; Hindley et al., 2015; Hoffmann et al., 2013, 2016; Sato et al., 2012; Trinh et al., 2018). Figure 1 shows the seasonal zonal-mean PE for each year and longitude-height variations of percentage of the relative seasonal mean PE (short for relative PE) at around 40°S during each NH summer from 2002 to 2017.

The seasonal zonal-mean PE exhibits year-to-year variations and increases exponentially with height (see left column of Figure 1), especially in the upper stratosphere and lower mesosphere (z ~ 30–70 km). In order to see the variations "equally" at all altitudes and to highlight the longitudinal variations, we show the relative PE in columns 2–5 of Figure 1. For ease of comparison, we also overplot the seasonal mean zonal wind and the average topographic elevations.

From Figure 1, we see that the relative PE each year always has a peak at around 60–80°W, which is just above and east of the Andes mountains (Becker & Vadas, 2018; de Wit et al., 2017; Sato et al., 2012). The features of these peaks can be described by their magnitudes and vertical extents. The magnitudes of the peaks exceed 80% in most years. Specifically, the peaks of the relative PE are 80% in 2008 and 2011 and reach 160% in 2010. Noted that in 2006, the peak is not as strong as in other years. The vertical extents of the peaks vary from year to year and extend to about z ~ 60 km in most years. Compared to the strong peaks below z ~ 60 km, the peaks are weaker and somewhat more "spread out" longitudinally above z ~ 60 km. These weak peaks have a westward tilt west of 80°W above z ~ 60 km. We note that the vertical extent of the peak is only up to about z ~ 40 km in 2006, 2009, and 2016. This might be due to interannual variations of either the wave sources (e.g., the strength of the wind blowing over the Andes) or the atmospheric environment that the MWs propagate in (e.g., the strength of the stratospheric jet). If the initial MW amplitudes are very large or the jet is weak, then the MWs will not penetrate very far into the stratosphere before breaking.

Further examination of Figure 1 shows that there is a transition region whereby the magnitude of the relative PE decreases and then increases again. This important transition region varies from year to year and occurs at z ~ 55 km to z ~ 65 km in most years. This decrease was shown in Figure 2 of Trinh et al. (2018). The altitude where this decrease occurs is where the primary orographic waves typically break and deposit their momentum, thereby creating local body forces in the transition region (Becker & Vadas, 2018). Because

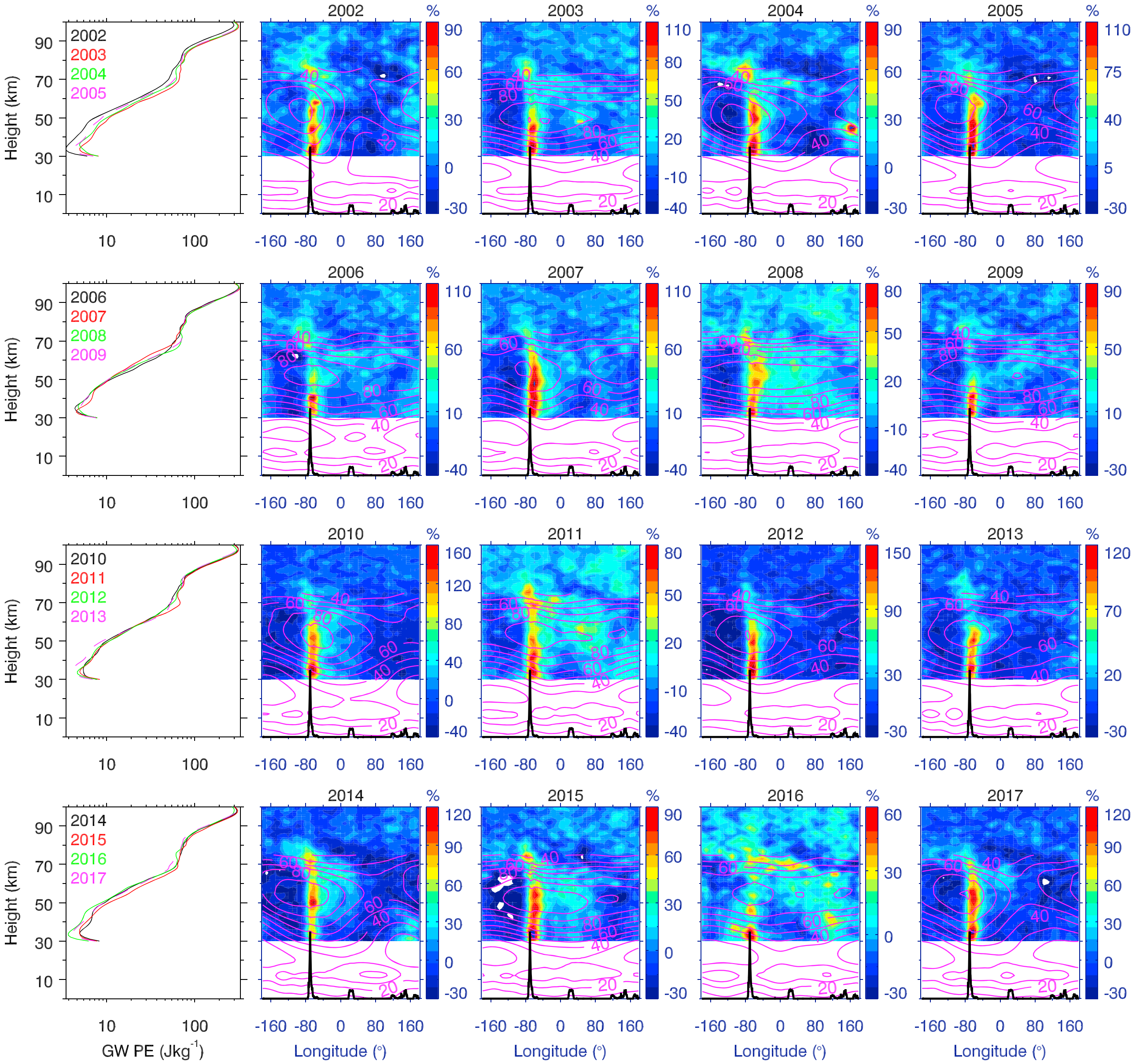

Figure 1. Seasonal zonal-mean PE (the leftmost column) and longitude-height distributions of the relative seasonal mean PE in each year (color-filled contours in the right four columns, in percent) at around 40°S and during the NH summer (June, July, and August) from 2002 to 2017. Also plotted in each panel is the seasonal mean zonal wind calculated from the Modern Era Retrospective analysis for Research and Applications 2 and averaged over the same season and latitude band as that for PE (the magenta contour lines in the right four columns with contour interval of 10 m/s; the solid and dashed contour lines represent the eastward and westward winds, respectively). The average topographic elevations (multiplied by a factor of 20 for readability) at around 40°S are shown as black lines at the bottom of each panel. The seasonal zonal-mean PE during each year is indicated by a different color. Note that the color scale for the relative PE differs from year to year to highlight the longitudinal variations for each year. PE = potential energy per unit mass.

local body forces generate LSWs that propagate upward and downward away from the body forces (Vadas et al., 2003, 2018), we suggest that the increase of the relative PE occurs where the secondary GWs have a large-enough amplitude to be observed by SABER. From the seasonal zonal-mean PE shown in Figure 1, we see that this quantity does not increase exponentially with height from z ~ 65 km to z ~ 80 km. This is likely due to the dissipation of some of the secondary GWs (Becker & Vadas, 2018), as well as to the fact that the secondary GW amplitudes are relatively weak below z ~ 80 km. This latter point coincides with the simulation studies of Vadas and Becker (2018), who found that the secondary GW amplitudes at z ~ 50–80 km were smaller than that of the primary GW amplitudes at z ~ 50 km. The smaller secondary

GW amplitudes occur because most of the momentum deposited into the background flow from primary GW breaking drives a mean flow response, thereby resulting in small initial secondary GW amplitudes.

A general feature of the zonal wind shown in Figure 1 is that it increases with height in the stratosphere and has a peak at $z \sim 50$ km (polar stratospheric jet) above the Andes. During a strong MW event, the eastward zonal wind increases with time in the stratosphere; this causes the MWs to be swept or advected downstream east of the Andes (Becker & Vadas, 2018; de Wit et al., 2017; Sato et al., 2012; Vadas & Becker, 2018). This causes the longitudinal gradient of the relative PE to be sharper west of (rather than east of) the Andes. Comparing the transition region and the vertical structure of the polar stratospheric jet, the lower boundary of the transition region coincides with the peak of the stratospheric jet. Above the transition region, the GWs appear in a wider longitudinal range. This is due to LSWs, because they propagate in all directions from the body forces (except perpendicular to the force; Vadas et al., 2003, 2018).

According to linear theory, the λ_z of a MW depends on the zonal wind ($u_0(z)$) as

$$\lambda_z = 2\pi u_0(z)/N_b.$$

Thus, λ_z increases as the eastward zonal wind increases with height. The vertical group velocity (c_{gz}) of a MW can be written as (Nappo, 2002)

$$c_{gz} = u_0(z)(\lambda_x\lambda_z)/\left(\lambda_x^2 + \lambda_z^2\right)$$

Simple calculation shows that an increasing $u_0(z)$ results in larger λ_z and c_{gz}. The waves with longer λ_z will be observed more easily by the limb scans of the SABER measurement mode and our method of extracting GWs, while the waves with faster c_{gz} will propagate to higher heights. This might contribute to the strong peak of the relative PE above the Andes. Above the peak height of the stratospheric jet, the zonal wind decreases with height. This causes the λ_z to decrease and the intrinsic horizontal phase speeds to decrease, which typically results in the MW quickly reaching convective instability and breaking. This agrees with the location of the transition region. Subsequently, local body forces created by the momentum deposition that occurs during MW breaking generate upward and downward-propagating LSWs. Because the secondary GWs initially have much smaller amplitudes than the primary GWs, those propagating downward will not be seen by SABER. However, because of the decreasing background density with altitude, those propagating upward (either eastward or westward) will increasingly be observed by SABER.

An important feature of Figure 1 is that there is a westward tilt of the secondary GWs during most of the years (e.g., at $z \sim 60$–80 km in 2012–2015). This westward tilt is in the direction of the large-scale wind shear, because the strong eastward wind in the stratosphere decelerates rapidly at these altitudes. This tilt is understood as follows. Eastward and westward LSWs are excited symmetrically in a frame moving eastward at the location of the body force (i.e., close to the peak of the stratospheric jet). In that reference frame, their intrinsic phase speeds (not their ground-based phase speeds) are symmetric about 0 m/s. As these waves propagate upward, the decreasing eastward wind applies a net westward wind on these waves (relative to the wind at their excitation altitude), which causes λ_z and the intrinsic frequencies of the westward (eastward) LSWs to decrease (increase). According to equation (14) of Vadas and Liu (2009), this causes the temperature perturbations of the westward (eastward) secondary GWs to increase (decrease) with height, which results in the westward tilt of the relative PE at $z \sim 60$–80 km seen in Figure 1. Note that effect causes the westward secondary GWs to break and attenuate below the altitude where the eastward secondary GWs break and attenuate (Becker & Vadas, 2018).

Figure 2 shows the 16-year-averaged relative monthly mean PE each month at around 40°S in order to illustrate the months where the longitudinal variations of GWs occur. The corresponding monthly mean zonal wind is also overplotted. We see that the relative PEs have prominent peaks in the longitude range of 60–80°W from April to October. Their magnitudes vary from month to month and exceed 60% from April to October. The maximum value of 130% occurs during June and September but not during July and August. This might be related to the fact that the GW generation over the oceans from spontaneous emission is strongest during July and August (Figures 13 and 14 of Ern et al., 2018). This imposes a stronger zonal-mean component of the GW activity during July–August. As a result, the relative importance of the GW orographic hot spot is weaker during those months, even though the absolute GW activity over the Southern Andes is likely stronger during July and August than during June and September (Hoffmann et al., 2016).

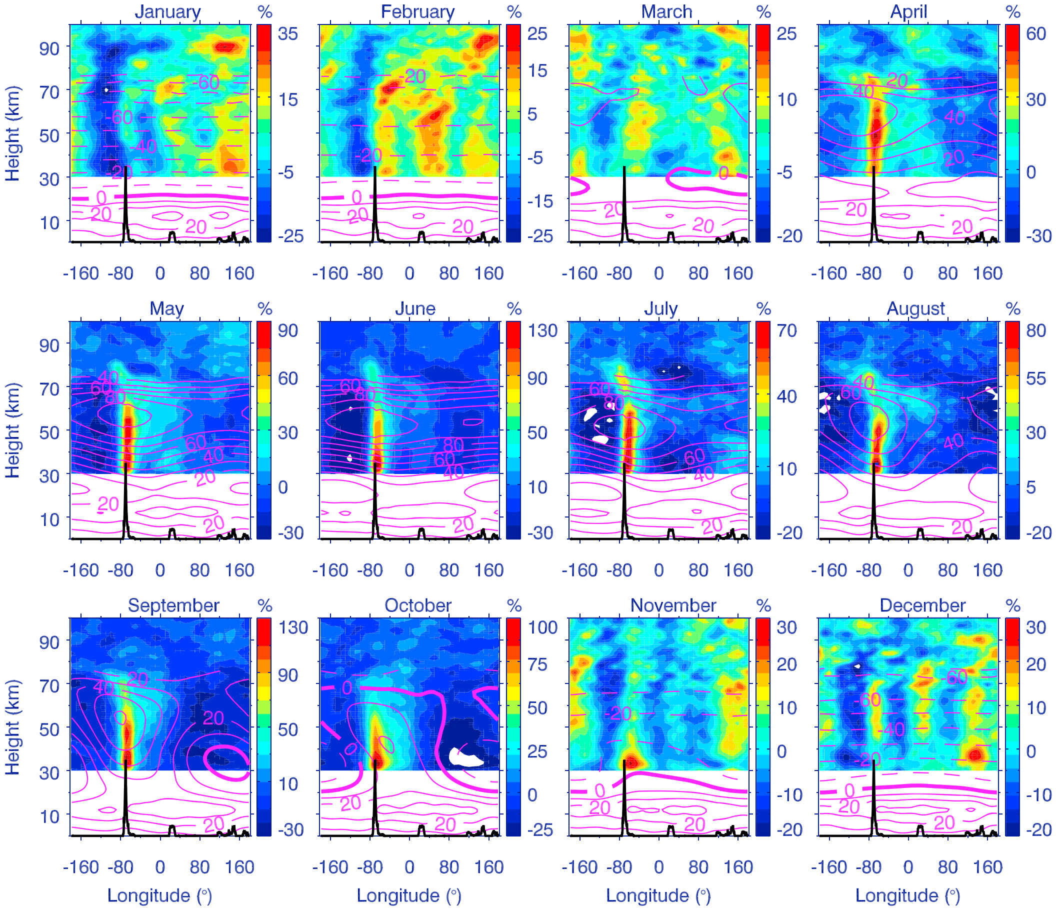

Figure 2. Longitude-height contours of the 16-year-averaged relative monthly mean PE (color-filled contours, in percent) at around 40°S. Also plotted in each panel is the monthly mean zonal wind at around 40°S calculated from the Modern Era Retrospective analysis for Research and Applications 2 and averaged over the 16 years (the magenta contour lines with contour interval of 10 m/s). The solid and dash contour lines represent the eastward and westward winds, respectively. The zero wind is indicated by a dark solid magenta line. The average elevations (multiplied by a factor of 20 for readability) in the latitude band of 40°S is shown as a black line in the bottom of each panel. The 16-year-averaged relative monthly mean PE is obtained by averaging the relative monthly PE in the same month over the 16-year. The relative monthly mean PE is defined in a similar manner as the relative seasonal mean PE but within a monthly time scale. Note that the color scale for the relative PE differs from month to month to highlight the longitudinal variations. PE = potential energy per unit mass.

The peaks extend to $z \sim 80$ km from April to October. However, the peaks above 60 km are weaker than those below 50 km during these months.

Upon careful examination of the vertical structure of the relative PE, we see a transition region whereby the magnitude of the peak of the relative PE decreases with height and then increases again. This transition region varies from month to month and generally occurs at $z \sim 55$–60 km (where the relative PE begins to decrease) and occurs at $z \sim 65$–70 km (where the relative PE begins to increase). This is similar to the situation for the relative PE shown in Figure 1. Comparing to the vertical structure of zonal wind, we find that the transition region is located just about the peak height of the stratospheric jet. In the transition region, the orographic waves break, create body forces, and excite LSWs. Note that the upward propagating LSWs form a wide peak longitudinally above the transition region (see Figure 2). As in Figure 1, there is a prominent westward tilt of the LSWs from April–September due to the decrease in the eastward wind with height.

Comparing the result for each summer (Figure 1) with the 16-year-averaged relative monthly mean PE (Figure 2) at 40°S, we see that the prominent weak LSWs peak above the transition region ($z > 65$ km) always exists, at least on a time scale of 16 years. Thus, this is a persistent longitudinal structure that is related to the specific orography of the Andes mountains and the polar stratospheric jet in this latitude band during these months.

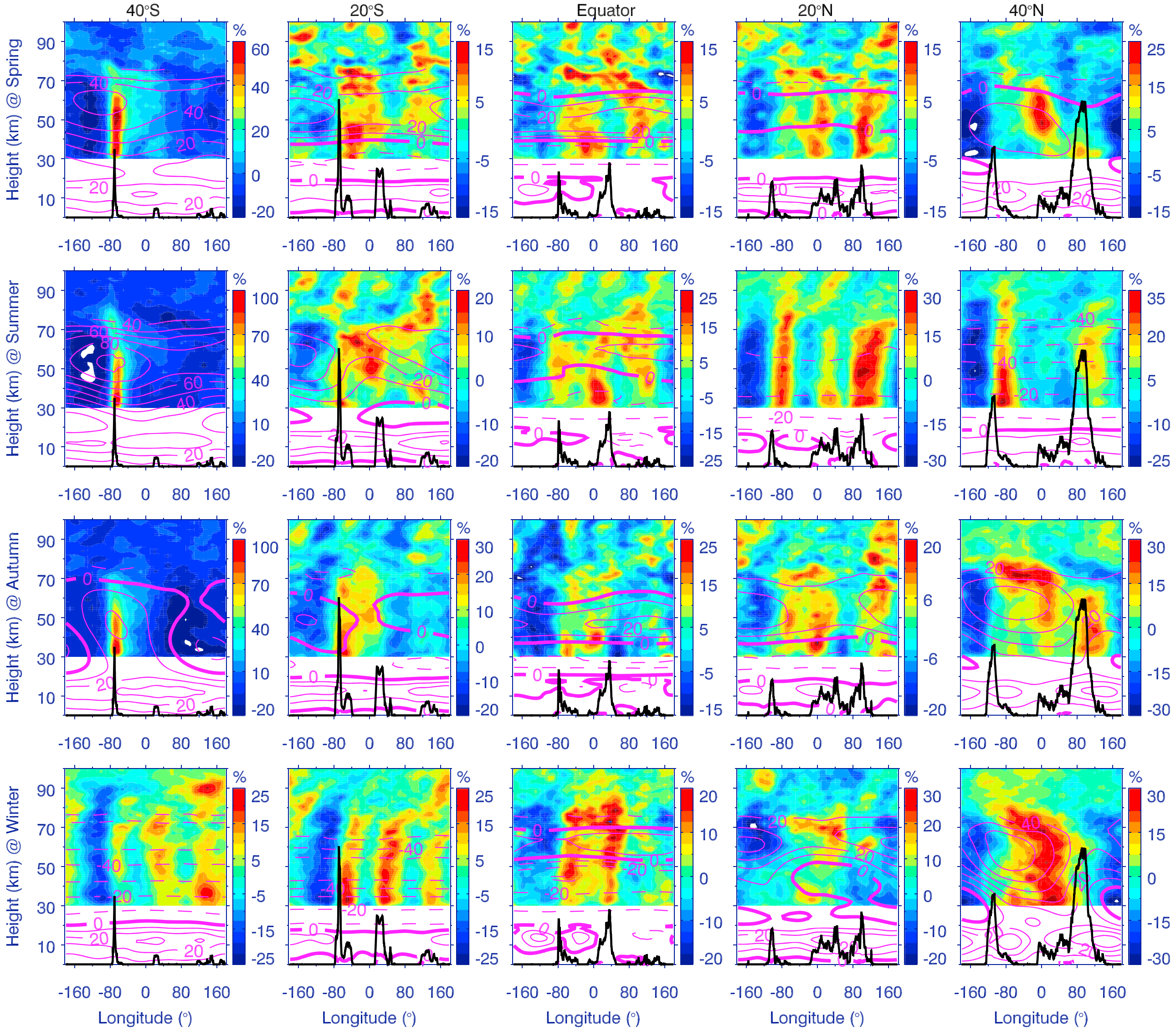

Figure 3. Longitude-height distributions of the 16-year-averaged relative seasonal mean PE (color, in percent) in five latitude bands (from left to right: 40°S, 20°S, equator, 20°N, and 40°N) and four seasons (from upper to lower panel: NH spring, NH summer, NH autumn, and NH winter). Also plotted in each panel is the seasonal mean zonal wind calculated from the Modern Era Retrospective analysis for Research and Applications 2 and averaged over the same season and latitude band as that for PE (the magenta contour lines with contour interval of 10 m/s; the solid and dash contour lines represent the eastward and westward winds respectively; the zero wind is indicated by a bold solid line). The averaged elevations in each latitude band (multiplied by a factor of 20 for better readability) are plotted as a black line in the bottom of each panel. The 16-year-averaged relative seasonal mean PE is obtained by averaging the relative seasonal mean PE in the same season for 16 years. Note that the color scale for the relative PE differs among the panels to better highlight the longitudinal variations. PE = potential energy per unit mass; NH = Northern Hemisphere.

In contrast to the prominent peaks in the longitude range of 60–80°W from April to October, the peaks are relatively weak (<35% in all altitudes) during other months (January–March, November, and December). These weak peaks are centered at around 70°W, 30°E, and 150°E.

3.2. Global Distributions of the GW PE and the Larger-Scale Secondary GWs

Figure 3 shows the longitude-height distributions of the 16-year-averaged relative PE in the five latitude bands for the four seasons. For convenience, we plot the seasonal mean zonal wind and the average elevations in each season and latitude band.

We first concentrate on the relative PE at 40°S during the four seasons. There is a prominent peak above the Andes in the NH spring, summer, and autumn. This coincides with the prominent wintertime peak (NH summer) above the Andes in almost all the 16 years in Figure 1. This also coincides with the prominent peak above the Andes from April to October in Figure 2. The prominent peak above the Andes extends to a higher height in the NH spring and summer than during the NH autumn. Moreover, there are transition regions of the relative PE in the NH spring and summer. The minima of the relative PE in the transition region are at $z \sim 70$ km ($z \sim 65$ km) in the NH spring (summer). Above the transition region, the relative PE becomes wider in longitude due to the upward propagation of the LSWs. Note the westward tilt of the LSWs in NH spring and summer due to the decreasing eastward wind. During NH winter, the peak over the Andes is much weaker than during the other three seasons. This is likely caused by the wind reversal at $z \sim 20$ km, which acts as a critical level and prohibits the upward propagation of orographic GWs. There are two other peaks at around 30°E and 150°E, which have similar magnitudes as that over the Andes. These peaks are presumably related to the weak GW hot spots over South Africa and Tasmania. Note that a peak over New Zealand (at 180°E) is missing in this representation.

At around 40°N, there is a prominent peak at 40°W to 40°E in the NH spring and winter. The peak in the NH winter extends to $z \sim 80$ km and then shifts west of 60°W. Moreover, the peak in the NH winter is larger than that in spring. The longitude structures of the relative PE in NH spring and winter do not coincide with the topography at around 40°N. Thus, these GWs might not be generated by topography but might instead be generated by the tropospheric jet occurring at $z \sim 10$ km. In the NH summer the relative PE have two peaks which are east of two topography peaks (Rockies and Tibetan Plateau). Comparing with the zonal wind in the summer, we suggest that these two peaks might be caused in large part by the LSWs from MW breaking. In this scenario, the eastward zonal wind flows over the two topography peaks (Rockies and Tibetan Plateau) and generates orographic GWs. If the eastward wind accelerates in time, then the MWs will be swept downstream (Vadas & Becker, 2018). The MWs would then break and deposit their momentum downstream at $z \sim 20$ km where the wind reversal occurs. This would generate LSWs, some of which would propagate upward and create the peaks seen east of the topographic peaks in Figure 3. It is also possible that the peak east of the Rockies was caused in part by GWs from deep convection, because there is a summertime convective hot spot there in the Atmospheric Infrared Sounder data (Hoffmann et al., 2013; Hoffmann & Alexander, 2010). However, the minimum λ_x that SABER can observe is 300 km, which is much larger than that of the GWs typically excited by thunderstorms. Therefore, the GWs that SABER observes are unlikely to be dominated by GWs from deep convection.

At around 20°N, the relative PE has three peaks centered at around 80°W, 20°E, and 110°E; these peaks are much stronger during the NH summer than during the NH spring and autumn. These three peaks are located at and eastward of the topographic peaks, which are Mexico (~80°W), Northern Africa (~20°E), and Southern Asia (110°E). They are related to the regions of maximum moist convection during these seasons. Since these regions shift to the south during the NH winter, the corresponding peaks in the relative PE are not visible during the NH winter.

At around 20°S and during the NH winter, three peaks in the relative PE occur near 70°W (North Andes), 40°E (central Africa), and 150°E (Australia). This is similar to those at around 40°S in the NH winter and at 20°N in the NH summer. These peaks coincide with those in from satellite observations (Jiang, Wang, et al., 2004; Wu & Eckermann, 2008). It should be noted that the peak at around 20°S and 70°W exists in three seasons (NH spring, autumn, and winter) and is likely a combination of orographic and convective GW sources.

Summarizing, at low latitudes, the longitudinal variations of the relative PE are not consistent with that of the topography, except for the peak at around 70°W during the NH winter. This may be because of the following: (1) The main GW source near the equator is deep tropical convection (Ern et al., 2011; Ern & Preusse, 2012; Jiang, Wang, et al., 2004; Wu & Eckermann, 2008). (2) The longitude and height variations of the zonal winds are complex and are not favorable for the upward propagation of orographic GWs.

4. Summary

The global temperature profiles measured by the SABER instrument during the past 16 years (2002–2017) were used to study the global distributions of the orographic GWs and the associated LSWs, as well as their latitudinal and seasonal dependencies. To evaluate the mechanisms, we also utilized the zonal wind from the Modern Era Retrospective analysis for Research and Applications 2 and topography data from GTOP30.

At around 40°S and in each NH summer of 2002–2017, the GWs had a strong peak over the Andes mountains that extended to $z \sim 55$ km. Above this altitude, a transition region occurred whereby the PE decreased then increased again up to $z \sim 90$ km. We can understand these features as follows. The peak below $z \sim 55$ km was formed by the primary orographic GWs, which propagated upward to the stratopause region. At $z \sim 55$–65 km, the primary orographic GWs broke and deposited their momentum into the mean flow. This resulted in the creation of local body forces, which unbalanced the mean flow. As a result, LSWs were generated. Those which propagated upward created the wide GW peak above $z \sim 65$ km. GW propagation, breaking, and the generation of secondary GWs was seen from April to October at 40°S. During the Southern Hemisphere winter of the Andes, we also found that orographic GWs broken just above the peak height of the stratospheric jet at 40°S.

At around 40°N during the NH summer, GWs peaked above the topographic regions (at $z \geq 30$ km), while nonorographic GW sources were important for the longitudinal structure during the NH winter. Because the orographic GWs likely broke where the wind reversal occurred at lower altitudes, we hypothesize that the SABER GWs at middle latitudes during the NH summer are LSWs generated by the body forces created by primary orographic GW breaking at $z \sim 20$ km. At low latitudes, we found that a combination of convective and orographic GW generation explains the GW peaks seen in the middle atmosphere.

In conclusion, we find that both the primary orographic GWs and the associated LSWs are responsible for the persistent global distribution of GWs. We note that both the primary and LSWs studied here have λ_z of 5–30 km and λ_x ranging from 300 to ~3,200–5,000 km. These GWs only occupy part of the GW spectra. To fully understand the global distributions of GWs, GW-resolving model simulations and observations are needed, especially in orographic hot spot regions such as the Andes and the Tibetan Plateau.

Acknowledgments
We thank Dong Wu for helpful discussions. The SABER data were obtained from ftp://saber.gats-inc.com/Version2_0/Level2A/ website. The topographic data were obtained from http://www.webgis.com/terr_world.html website. The wind data were obtained from http://disc.sci.gsfc.nasa.gov/mdisc/ website. This work was supported by the National Natural Science Foundation of China (41874182, 41831073, 41574143, and 41331069) and the Educational Commission of Henan Province of China (17HASTIT010). This work was also supported in part by the Specialized Research Fund and the Open Research Program of the State Key Laboratory of Space Weather. S. L. V. was supported by NSF Grants AGS-1832988 and AGS-1552315.

References

Alexander, M. J., Geller, M., McLandress, C., Polavarapu, S., Preusse, P., Sassi, F., et al. (2010). Recent developments in gravity-wave effects in climate models and the global distribution of gravity-wave momentum flux from observations and models. *Quarterly Journal of the Royal Meteorological Society*, *136*, 1103–1124.

Alexander, M. J., Gille, J., Cavanaugh, C., Coffey, M., Craig, C., Eden, T., et al. (2008). Global estimates of gravity wave momentum flux from high resolution dynamics limb sounder observations. *Journal of Geophysical Research*, *113*, D15S18. https://doi.org/10.1029/2007JD008807

Alexander, M. J., & Teitelbaum, H. (2007). Observation and analysis of a large amplitude mountain wave event over the Antarctic Peninsula. *Journal of Geophysical Research*, *112*, D21103. https://doi.org/10.1029/2006JD008368

Alexander, M. J., & Teitelbaum, H. (2011). Three-dimensional properties of Andes mountain waves observed by satellite: A case study. *Journal of Geophysical Research*, *116*, D23110. https://doi.org/10.1029/2011JD016151

Alexander, S. P., Klekociuk, A. R., & Tsuda, T. (2009). Gravity wave and orographic wave activity observed around the Antarctic and Arctic stratospheric vortices by the COSMIC GPS-RO satellite constellation. *Journal of Geophysical Research*, *114*, D17103. https://doi.org/10.1029/2009JD011851

Baumgaertner, A. J. G., & McDonald, A. J. (2007). A gravity wave climatology for Antarctica compiled from Challenging Minisatellite Payload/Global Positioning System (CHAMP/GPS) radio occultations. *Journal of Geophysical Research*, *112*, D05103. https://doi.org/10.1029/2006JD007504

Becker, E., & Vadas, S. L. (2018). Secondary gravity waves in the winter mesosphere: Results from a high-resolution global circulation model. *Journal of Geophysical Research: Atmospheres*, *123*, 2605–2627. https://doi.org/10.1002/2017JD027460

Bossert, K., Kruse, C. G., Heale, C. J., Fritts, D. C., Williams, B. P., Snively, J. B., et al. (2017). Secondary gravity wave generation over New Zealand during the DEEPWAVE campaign. *Journal of Geophysical Research: Atmospheres*, *122*, 7834–7850. https://doi.org/10.1002/2016JD026079

Bruinsma, S. L., & Forbes, J. M. (2008). Medium to large-scale density variability as observed by CHAMP. *Space Weather*, *6*, S08002. https://doi.org/10.1029/2008SW000411

Chu, X., Zhao, J., Lu, X., Harvey, V. L., Jones, R. M., Becker, E., et al. (2018). Lidar observations of stratospheric gravity waves from 2011 to 2015 at McMurdo (77.84°S, 166.69°E), Antarctica: 2. Potential energy densities, lognormal distributions, and seasonal variations. *Journal of Geophysical Research: Atmospheres*, *123*, 7910–7934. https://doi.org/10.1029/2017JD027386

de Wit, R. J., Janches, D., Fritts, D. C., Stockwell, R. G., & Coy, L. (2017). Unexpected climatological behavior of MLT gravity wave momentum flux in the lee of the Southern Andes hot spot. *Geophysical Research Letters*, *44*, 1182–1191. https://doi.org/10.1002/2016GL072311

Eckermann, S. D., & Preusse, P. (1999). Global measurements of stratospheric mountain waves from space. *Science*, *286*(5444), 1534–1537. https://doi.org/10.1126/science.286.5444.1534

Ern, M., Ploeger, F., Preusse, P., Gille, J. C., Gray, L. J., Kalisch, S., et al. (2014). Interaction of gravity waves with the QBO: A satellite perspective. *Journal of Geophysical Research: Atmospheres*, *119*, 2329–2355. https://doi.org/10.1002/2013JD020731

Ern, M., & Preusse, P. (2012). Gravity wave momentum flux spectra observed from satellite in the summertime subtropics: Implications for global modeling. *Geophysical Research Letters*, *39*, L15810. https://doi.org/10.1029/2012GL052659

Ern, M., Preusse, P., Gille, J. C., Hepplewhite, C. L., Mlynczak, M. G., Russell, J. M. III, & Riese, M. (2011). Implications for atmospheric dynamics derived from global observations of gravity wave momentum flux in stratosphere and mesosphere. *Journal of Geophysical Research*, *116*, D19107. https://doi.org/10.1029/2011JD015821

Ern, M., Trinh, Q. T., Preusse, P., Gille, J. C., Mlynczak, M. G., Russell, J. M. III, & Riese, M. (2018). GRACILE: A comprehensive climatology of atmospheric gravity wave parameters based on satellite limb soundings. *Earth System Science Data*, *10*(2), 857–892. https://doi.org/10.5194/essd-10-857-2018

Forbes, J. M., Bruinsma, S. L., Doornbos, E., & Zhang, X. (2016). Gravity wave-induced variability of the middle thermosphere. *Journal of Geophysical Research: Space Physics*, *121*, 6914–6923. https://doi.org/10.1002/2016JA022923

Fritts, D. C., & Alexander, M. J. (2003). Gravity wave dynamics and effects in the middle atmosphere. *Reviews of Geophysics*, *41*(1), 1003. https://doi.org/10.1029/2001RG000106

Fritts, D. C., Smith, R. B., Taylor, M. J., Doyle, J. D., Eckermann, S. D., Dörnbrack, A., et al. (2016). The Deep Propagating Gravity Wave Experiment (DEEPWAVE): An airborne and ground-based exploration of gravity wave propagation and effects from their sources throughout the lower and middle atmosphere. *Bulletin of the American Meteorological Society*, *97*(3), 425–453. https://doi.org/10.1175/BAMS-D-14-00269.1

Gelaro, R., McCarty, W., Suárez, M. J., Todling, R., Molod, A., Takacs, L., et al. (2017). The Modern-Era Retrospective Analysis for research and applications, version 2 (MERRA-2). *Journal of Climate*, *30*(14), 5419–5454. https://doi.org/10.1175/JCLI-D-16-0758.1

Geller, M. A., Alexander, M. J., Love, P. T., Bacmeister, J., Ern, M., Hertzog, A., et al. (2013). A comparison between gravity wave momentum fluxes in observations and climate models. *Journal of Climate*, *26*(17), 6383–6405. https://doi.org/10.1175/JCLI-D-12-00545.1

Gong, J., Wu, D. L., & Eckermann, S. D. (2012). Gravity wave variances and propagation derived from AIRS radiances. *Atmospheric Chemistry and Physics*, *12*(4), 1701–1720. https://doi.org/10.5194/acp-12-1701-2012

Gong, J., Yue, J., & Wu, D. L. (2015). Global survey of concentric gravity waves in AIRS images and ECMWF analysis. *Journal of Geophysical Research: Atmospheres*, *120*, 2210–2228. https://doi.org/10.1002/2014JD022527

Heale, C. J., Bossert, K., Snively, J. B., Fritts, D. C., Pautet, P. D., & Taylor, M. J. (2017). Numerical modeling of a multiscale gravity wave event and its airglow signatures over Mount Cook, New Zealand, during the DEEPWAVE campaign. *Journal of Geophysical Research: Atmospheres*, *122*, 846–860. https://doi.org/10.1002/2016JD025700

Hindley, N. P., Wright, C. J., Smith, N. D., & Mitchell, N. J. (2015). The southern stratospheric gravity wave hot spot: Individual waves and their momentum fluxes measured by COSMIC GPS-RO. *Atmospheric Chemistry and Physics*, *15*(14), 7797–7818. https://doi.org/10.5194/acp-15-7797-2015

Hoffmann, L., & Alexander, M. J. (2010). Occurrence frequency of convective gravity waves during the north American thunderstorm season. *Journal of Geophysical Research*, *115*, D20111. https://doi.org/10.1029/2010JD014401

Hoffmann, L., Grimsdell, A. W., & Alexander, M. J. (2016). Stratospheric gravity waves at Southern Hemisphere orographic hotspots: 2003–2014 AIRS/Aqua observations. *Atmospheric Chemistry and Physics*, *16*(14), 9381–9397. https://doi.org/10.5194/acp-16-9381-2016

Hoffmann, L., Xue, X., & Alexander, M. J. (2013). A global view of stratospheric gravity wave hotspots located with Atmospheric Infrared Sounder observations. *Journal of Geophysical Research: Atmospheres*, *118*, 416–434. https://doi.org/10.1029/2012JD018658

Jiang, J. H., Eckermann, S. D., Wu, D. L., & Ma, J. (2004). A search for mountain waves in MLS stratospheric limb radiances from the winter Northern Hemisphere: Data analysis and global mountain wave modeling. *Journal of Geophysical Research*, *109*, D03107. https://doi.org/10.1029/2003JD003974

Jiang, J. H., Wang, B., Goya, K., Hocke, K., Eckermann, S. D., Ma, J., et al. (2004). Geographical distribution and interseasonal variability of tropical deep convection: UARS MLS observations and analyses. *Journal of Geophysical Research*, *109*, D03111. https://doi.org/10.1029/2003JD003756

John, S. R., & Kumar, K. K. (2012). TIMED/SABER observations of global gravity wave climatology and their interannual variability from stratosphere to mesosphere lower thermosphere. *Climate Dynamics*, *39*(6), 1489–1505. https://doi.org/10.1007/s00382-012-1329-9

Liu, H.-L. (2000). Temperature changes due to gravity wave saturation. *Journal of Geophysical Research*, *105*(D10), 12,329–12,336. https://doi.org/10.1029/2000JD900054

Liu, H.-L. (2016). Variability and predictability of the space environment as related to lower atmosphere forcing. *Space Weather*, *14*, 634–658. https://doi.org/10.1002/2016SW001450

Liu, H.-L., Bardeen, C. G., Foster, B. T., Lauritzen, P., Liu, J., Lu, G., et al. (2018). Development and validation of the Whole Atmosphere Community Climate Model with thermosphere and ionosphere extension (WACCM-X 2.0). *Journal of Advances in Modeling Earth Systems*, *10*(2), 381–402. https://doi.org/10.1002/2017MS001232

Liu, H. L., & Vadas, S. L. (2013). Large-scale ionospheric disturbances due to the dissipation of convectively-generated gravity waves over Brazil. *Journal of Geophysical Research: Space Physics*, *118*, 2419–2427. https://doi.org/10.1002/jgra.50244

Liu, H.-X., Pedatella, N., & Hocke, K. (2017). Medium-scale gravity wave activity in the bottomside F region in tropical regions. *Geophysical Research Letters*, *44*, 7099–7105. https://doi.org/10.1002/2017GL073855

Liu, X., Xu, J., Liu, H.-L., & Ma, R. (2008). Nonlinear interactions between gravity waves with different wavelengths and diurnal tide. *Journal of Geophysical Research*, *113*, D08112. https://doi.org/10.1029/2007JD009136

Liu, X., Yue, J., Xu, J., Garcia, R. R., Russell, J. M. III, Mlynczak, M. G., et al. (2017). Variations of global gravity waves derived from 14 years of SABER temperature observations. *Journal of Geophysical Research: Atmospheres*, *122*, 6231–6249. https://doi.org/10.1002/2017JD026604

Molod, A., Takacs, L., Suarez, M., & Bacmeister, J. (2015). Development of the GEOS-5 atmospheric general circulation model: Evolution from MERRA to MERRA2. *Geoscientific Model Development*, *8*(5), 1339–1356. https://doi.org/10.5194/gmd-8-1339-2015

Nappo, C. J. (2002). *An introduction to atmospheric gravity waves* (pp. 47–84). San Diego, CA: Academic Press.

Park, J., Lühr, H., Lee, C., Kim, Y. H., Jee, G., & Kim, J.-H. (2014). A climatology of medium-scale gravity wave activity in the midlatitude/low-latitude daytime upper thermosphere as observed by CHAMP. *Journal of Geophysical Research: Space Physics*, *119*, 2187–2196. https://doi.org/10.1002/2013JA019705

Preusse, P., Dörnbrack, A., Eckermann, S. D., Riese, M., Schaeler, B., Bacmeister, J., et al. (2002). Space based measurements of stratospheric mountain waves by CRISTA: 1. Sensitivity, analysis method and a case study. *Journal of Geophysical Research*, *107*(D23), 8178. https://doi.org/10.1029/2001JD000699

Russell, J. M. III, Mlynczak, M. G., Gordley, L. L., Tansock, J., & Esplin, R. (1999). An overview of the SABER experiment and preliminary calibration results. *Proceedings of SPIE*, *3756*, 277–288.

Sato, K., Tateno, S., Watanabe, S., & Kawatani, Y. (2012). Gravity wave characteristics in the southern hemisphere revealed by a high-resolution middle-atmosphere general circulation model. *Journal of the Atmospheric Sciences*, *69*(4), 1378–1396. https://doi.org/10.1175/JAS-D-11-0101.1

Sato, K., Watanabe, S., Kawatani, Y., Tomikawa, Y., Miyazaki, K., & Takahashi, M. (2009). On the origins of mesospheric gravity waves. *Geophysical Research Letters*, *36*, L19801. https://doi.org/10.1029/2009GL039908

Trinh, Q. T., Ern, M., Doornbos, E., Preusse, P., & Riese, M. (2018). Satellite observations of middle atmosphere-thermosphere vertical coupling by gravity waves. *Annales Geophysicae*, *36*(2), 425–444. https://doi.org/10.5194/angeo-36-425-2018

Vadas, S. L. (2013). Compressiblef-plane solutions to body forces, heatings, and coolings, and application to the primary and secondary gravity waves generated by a deep convective plume. *Journal of Geophysical Research: Space Physics*, *118*, 2377–2397. https://doi.org/10.1002/jgra.50163

Vadas, S. L., & Becker, E. (2018). Numerical modeling of the excitation, propagation, and dissipation of primary and secondary gravity waves during wintertime at McMurdo Station in the Antarctic. *Journal of Geophysical Research: Atmospheres*, *123*, 9326–9369. https://doi.org/10.1029/2017JD027974

Vadas, S. L., & Fritts, D. C. (2002). The importance of spatial variability in the generation of secondary gravity waves from local body forces. *Geophysical Research Letters*, *29*(20), 1984. https://doi.org/10.1029/2002GL015574

Vadas, S. L., Fritts, D. C., & Alexander, M. J. (2003). Mechanism for the generation of secondary waves in wave breaking regions. *Journal of the Atmospheric Sciences*, *60*(1), 194–214. https://doi.org/10.1175/1520-0469(2003)060<0194:MFTGOS>2.0.CO;2

Vadas, S. L., & Liu, H.-L. (2009). The generation of large-scale gravity waves and neutral winds in the thermosphere from the dissipation of convectively-generated gravity waves. *Journal of Geophysical Research*, *114*, A10310. https://doi.org/10.1029/2009JA014108

Vadas, S. L., & Liu, H.-L. (2013). Numerical modeling of the large-scale neutral and plasma responses to the body forces created by the dissipation of gravity waves from 6 h of deep convection in Brazil. *Journal of Geophysical Research: Space Physics*, *118*, 2593–2617. https://doi.org/10.1002/jgra.50249

Vadas, S. L., Liu, H.-L., & Lieberman, R. S. (2014). Numerical modeling of the global changes to the thermosphere and ionosphere from the dissipation of gravity waves from deep convection. *Journal of Geophysical Research: Space Physics*, *119*, 7762–7793. https://doi.org/10.1002/2014JA020280

Vadas, S. L., Zhao, J., Chu, X., & Becker, E. (2018). The excitation of secondary gravity waves from local body forces: Theory and observation. *Journal of Geophysical Research: Atmospheres*, *123*, 9296–9325. https://doi.org/10.1029/2017JD027970

Watanabe, S., & Miyahara, S. (2009). Quantification of the gravity wave forcing of the migrating diurnal tide in gravity wave-resolving general circulation model. *Journal of Geophysical Research*, *114*, D07110. https://doi.org/10.1029/2008JD011218

Wu, D. L., & Eckermann, S. D. (2008). Global Gravity Wave Variances fromAuraMLS: Characteristics and Interpretation. *Journal of the Atmospheric Sciences*, *65*(12), 3695–3718. https://doi.org/10.1175/2008JAS2489.1

Wu, D. L., & Jiang, J. H. (2002). MLS observations of atmospheric gravity waves over Antarctica. *Journal of Geophysical Research*, *107*(D24), 4773. https://doi.org/10.1029/2002JD002390

Zhao, J., Chu, X., Chen, C., Lu, X., Fong, W., Yu, Z., et al. (2017). Lidar observations of stratospheric gravity waves from 2011 to 2015 at McMurdo (77.84°S, 166.69°E), Antarctica: 1. Vertical wavelengths, periods, and frequency and vertical wave number spectra. *Journal of Geophysical Research: Atmospheres*, *122*, 5041–5062. https://doi.org/10.1002/2016JD026368